Single-Bit All-Digital Frequency Synthesis Using Homodyne Sigma-Delta Modulation

Paul P. Sotiriadis, *Senior Member, IEEE*

***Abstract*— All-digital frequency synthesis using bandpass sigma-delta modulation to achieve spectrally clean single-bit output is presented and mathematically analyzed resulting in a complete model to predict the stability and output spectrum. The quadrature homodyne filter architecture is introduced resulting in efficient implementations of carrier-frequency-centered bandpass filters for the modulator. A multiplierless version of the quadrature homodyne filter architecture is also introduced to reduce complexity while maintaining a clean in-band spectrum. MATLAB and SIMULINK simulation results present the potential capabilities of the synthesizer architectures and validate the accuracy of the developed theoretical framework.**

***Index Terms*— Digital signal processing, digital-to-analog converter, digital-to-frequency converter, direct digital synthesis (DDS), feedback loop, filter, frequency spurs, frequency synthesis, noise shaping, quantization, sigma-delta modulation.**

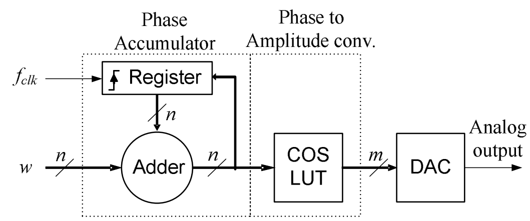

Fig. 1. Basic form of DDS.

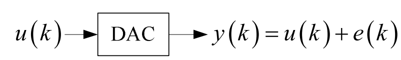

Fig. 2. DAC's output error.

I. Introduction

DIRECT all-digital frequency synthesizers *with single-bit output* are attractive for two main reasons.

One is the obvious: the design and operational advantages of fully digital circuits, especially with very large scale integration implementation in mind. Being digital, their design is supported by powerful design, verification, and layout automation tools, and once they have been designed, migrating them to newer integration technologies is done easily in contrast to their analog and mixed-signal counterparts that require careful redesign, a procedure becoming more and more challenging with technology downscaling. Moreover, digital RF blocks like all-digital frequency synthesizers may require less chip area and are easier to cointegrate with DSP engines. Digital circuits are less sensitive to noise and to temperature, supply, and process variations. In addition, all-digital frequency synthesizers with single-bit output have all the advantages of direct digital synthesizers (DDS) in Fig. 1 such as very high frequency resolution, fast frequency hopping, and direct modulation.

The other reason that makes single-bit-output all-digital frequency synthesizers attractive is that, under certain conditions, they can achieve higher dynamic range (DR) and spurious-free DR (SFDR) near-in than those of the standard DDS.

This is because although the standard DDS can synthesize signals with very high DR and SFDR in the digital domain, converting them into the analog domain with a multibit DAC degrades their spectral quality. DAC is challenging to design, very power hungry, and the main limiting factor in the DDS' SFDR due to its limited resolution in high sampling rates and its complex nonlinearity. Instead, all-digital frequency synthesizers with single-bit output directly convert the serial digital 0/1 output level into the analog domain. Having only two levels, the only possible errors of conversion are amplitude and offset, which have no impact on the spectral quality of the signal. Moreover, all-digital frequency synthesizers with single-bit output maintain the excellent residual phase noise and jitter performance of the standard DDS.

One may wonder how a single-bit DAC can result in better DR and SFDR than the multibit one. Consider Fig. 2 where the output of the DAC has an instantaneous error $e(k)$.

In the case of single-bit-output synthesizers, the output of the 1-b DAC is $y(k) = \mathrm{sgn}\big(u(k)\big)$ with high accuracy because of the nature of the conversion. Therefore, the error is known (in advance) to be $e(k) = \mathrm{sgn}\big(u(k)\big) - u(k)$. Sigma-delta ($\Sigma/\Delta$) modulation techniques allow us to feed the error back and make it (pseudo-) random and orthogonal to the desirable signal (e.g., sinusoidal) with a power spectrum outside the band of interest. In contrast, the error $e(k)$ in multibit DACs is not accurately known. This is partially because of the static nonlinearity of the DAC and mainly due to its dynamic errors, depending on previous states and synchronization glitches that are practically impossible to model with accuracy.

Early efforts to build single-bit-output DDS and eliminate the DAC date to at least 30 years back. A typical case is the pulse-DDS (PDDS) using the most significant bit of the

Manuscript received August 1, 2016; accepted September 8, 2016. Date of publication October 5, 2016; date of current version February 1, 2017. This work was partially supported by the Broadcom Foundation, USA.

The author is with the National Technical University of Athens, Greece (e-mail: pps@ieee.org).

Digital Object Identifier 10.1109/TUFFC.2016.2615271

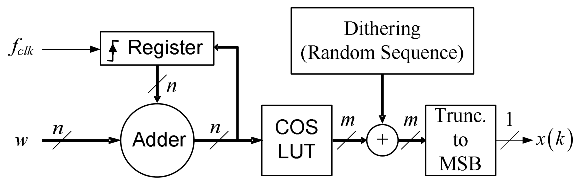

Fig. 3. PDDS with optional amplitude random dithering.

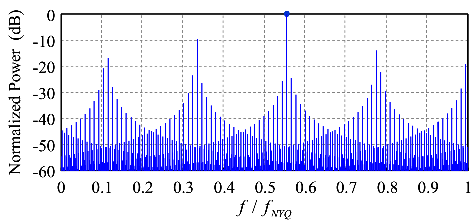

Fig. 4. Spectrum of undithered PDDS ($w = 2273$, $n = 13$).

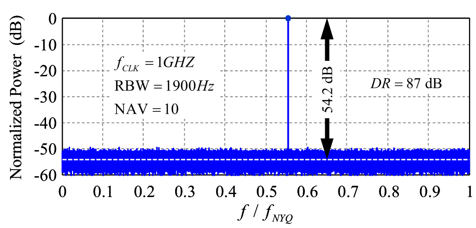

Fig. 5. Spectrum of dithered PDDS corresponding to that in Fig. 4.

sinusoidal look-up-table (LUT) as its output (Fig. 3, without dithering) [1]–[3]. PDDS is a finite state machine (FSM) with single-bit output (ignore dithering for now).

All-digital frequency synthesizers (without oscillators) are FSM driven by a clock whose rising and falling edges specify those of the output. The consequence of this is that only integral division frequencies of the clock produce a clean spectrum. For all other generated frequencies, the output waveform is irregular with a high deterministic jitter and a spectrum polluted with spurs that can be very close to the carrier, as in Fig. 4, for the case of PDDS ($f_{\text{NYQ}} = f_{\text{clk}}/2$).

Random dithering in PDDS can alleviate or completely eliminate spurs. The spectrum of dithered PDDS corresponding to that of Fig. 4 is shown in Fig. 5 [4].

Although dithering may remove spurs, it introduces noise that appears as noise floor. It can be shown that if white uniformly distributed dither of a certain amplitude is used, the spurs are eliminated and the DR [power of the carrier over the power spectral density (PSD) of the near-in noise] is of the order of $10\log_{10}(f_{\text{clk}})$. Dithering with colored random sequences improves the DR only marginally [5].

We get similar results (with and without dithering) from flying adder (FA)-type synthesizers, a class of all-digital period synthesizers in which the output average period is proportional to the frequency control word w [6]–[11].

The cases of PDDS and FA indicate that direct dithering cannot achieve a high DR in single-bit-output digital synthesizers. Therefore, feedback is required to shape the PSD of

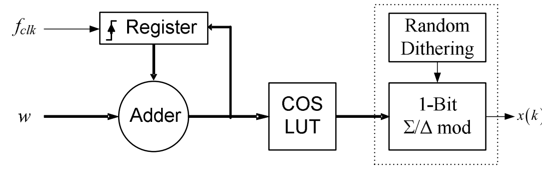

Fig. 6. Replacing multibit DAC of the DDS with a bandpass 1-b Σ/Δ modulator.

the noise away from the carrier. Σ/Δ modulation comes as a natural choice to achieve this.

Section II presents the concept of single-bit-output all-digital frequency synthesis based on Σ/Δ modulation. Section III uses quasi-linearization techniques to model the nonlinear behavior of the single-bit Σ/Δ modulator and derive its output spectrum. Section IV introduces the quadrature *homodyne* filter architecture resulting in efficient implementation of carrier-frequency-centered bandpass filters for the modulator. The multiplier-free variation of the quadrature *homodyne* filter is also introduced to reduce the complexity of the loop. Section V presents SIMULINK simulation results of the all-digital frequency synthesizer and compares them with those of the developed theory. Section VI concludes the paper.

II. Sigma-Delta Modulation for All-Digital Frequency Synthesis

The previous section discussed the difficulty of achieving high DR and SFDR from single-bit-output all-digital frequency synthesizers having a direct signal path structure, i.e., without feedback of the quantization errors. Feedback structures instead allow for very efficient noise shaping resulting in high DR and ideally a spurs-free band of interest [12]–[18]. The goal here is to generate a single-bit output sequence having a sinusoidal-like spectrum with a clean spectrum around it, useful for RF applications. Note, however, that this single-bit sequence may be, and typically is, very irregular in time and in most cases it cannot be used for clocking digital circuits.

To generate a single-bit sequence with a sinusoidal-like spectrum, we start with generating a multibit sinusoidal in the digital domain. We do so using a phase accumulator and a cosine LUT exactly as in the standard DDS, as shown in Fig. 6 but *without* a multibit DAC to convert it into analog.

Instead of the multibit DAC, we use a 1-b Σ/Δ modulator to convert the multibit stream of the *cosine* values in the digital domain into a sequence of ± 1 as shown in Fig. 7. We assume a general form of the Σ/Δ modulator with an extra gain g in the feedback path. Dithering sequence $d(k)$ is by construction zero-mean Gaussian white noise generated independently of any other signal. It has standard deviation σ_d and is used for eliminating any remaining spur.

The 1-b (± 1) quantization error is several orders of magnitude larger than that of the amplitude (and possibly phase) error of the cosine LUT representation of $A\cos(k\Omega)$ due to the finite resolution. Since the focus of this work is on the Σ/Δ modulator, we assume throughout this paper that $A\cos(k\Omega)$ is generated with sufficient accuracy so that its error is below our DR and SFDR target levels and therefore it can be ignored.

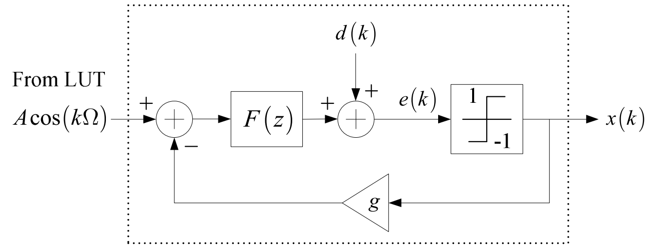

Fig. 7. Bandpass 1-b Σ/Δ modulator ($F(z)$ is bandpass).

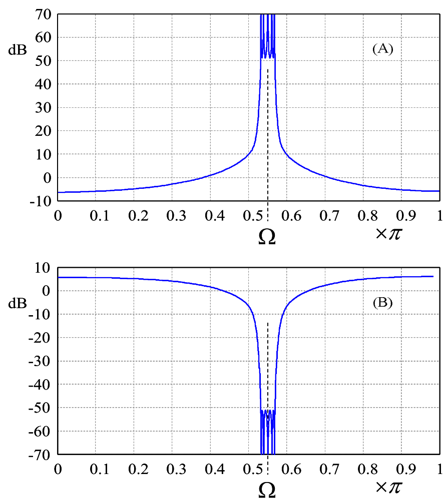

Fig. 8. (A) Typical $|F(e^{j\omega})|$ centered at $\Omega = 2\pi \cdot 2253/2^{13}$ and (B) the associated $ntf(z)$.

It is very common in the literature to replace the quantizer with the simple approximate equivalent of an additive quantization noise source $n(k)$ in order to derive the input–output behavior of the modulator. In this case, we obtain

$$X(z) = stf(z)U(z) + dtf(z)D(z) + ntf(z)N(z)$$

where $U(z)$ is the Z-transform of the input $A\cos(k\Omega)$

$$stf(z) = \frac{F(z)}{1 + gF(z)} \tag{1}$$

is the *signal transfer function*, and

$$dtf(z) = ntf(z) = \frac{1}{1 + gF(z)} \tag{2}$$

are the *dither* and *noise transfer functions* of the Σ/Δ modulator. This approximation of the quantizer is usually acceptable for multibit modulators but is not accurate for single-bit ones. In Section III, the quantizer is replaced by a more accurate quasi-linear model [19]. This results in a quasi-linear model of the modulator providing more accurate prediction of the PSD of the noise and the stability of the loop.

The bandpass transfer function $F(e^{j\omega})$ must attain large absolute values within the band of interest, around Ω, as in Fig. 8(A), in order to make $|stf(e^{j\omega})| \cong 1/g$ and $|ntf(e^{j\omega})|$ and $|dtf(e^{j\omega})|$ small, as illustrated in Fig. 8(B).

TABLE I
POLES AND ZEROS OF $F(z)$ USED IN SECTIONS III AND IV

POLES	ZEROS
-0.1223 ± 0.9925j	-7.4398
-0.1907 ± 0.9817j	-0.0705 ± 0.9601j
-0.1017 ± 0.9948j	-0.1066 ± 0.9541j
-0.2110 ± 0.9775j	-0.2292 ± 0.9348j
-0.1566 ± 0.9877j	-0.1937 ± 0.9400j

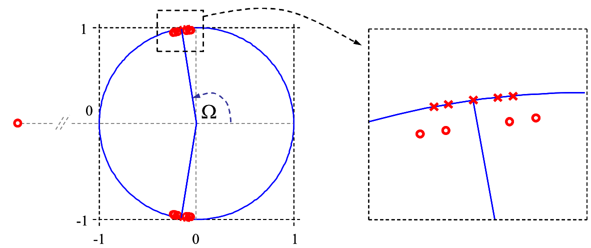

Fig. 9. Poles and zeros of $F(z)$ in Fig. 8(A) and Table I.

In Fig. 8 and in certain examples in Sections III and IV we consider the filter transfer function

$$F(z) = F_0 \cdot \frac{(z - z_1)(z - z_2)\ldots(z - z_{m_n})}{(z - p_1)(z - p_2)\ldots(z - p_{m_d})} \tag{3}$$

with poles and zeros as in Table I and gain $F_0 = -0.1566$.

Section IV illustrates how the bandpass $F(z)$ is realized using two identical low-pass transfer functions of lower order.

The poles of $F(z)$ must be accumulated around $e^{\pm j\Omega}$ and the zeros should be chosen to optimize noise suppression and guarantee stability of the loop [20]. The poles and zeros in Table I are shown in Fig. 9.

When the generated frequency Ω is fixed, or varies insignificantly with respect to the loop bandwidth, transfer function $F(z)$ is fixed and so are its coefficients. This allows us to round them and trade some accuracy for a significant reduction in the hardware complexity, primarily in multipliers that are the most power and area hungry building blocks.

When Ω varies significantly, it is desirable that $F(z)$ is tunable and tracks Ω to maintain high near-in DR [18]. In this case, rounding the coefficients of $F(z)$ parametrically on Ω to reduce hardware complexity is very challenging or practically impossible. This difficulty is resolved using the quadrature homodyne filter architecture introduced in Section IV.

III. MODULATOR'S NONLINEAR ANALYSIS

This section uses quasi-linearization theory [19] to model mathematically the nonlinear behavior of the single-bit Σ/Δ modulator used in the proposed all-digital frequency synthesis architecture. It derives the noise PSD and the DR near-in. A quasi-linear model of the quantizer is introduced first, since the quantizer is the nonlinear element in the loop. Based on it, the quasi-linear model of the modulator is derived.

A. Quasi-Linear Model of the Quantizer

Following the assumptions typically used in analyzing the nonlinear loop of the modulator in Fig. 7, the quantization

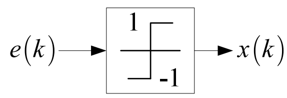

Fig. 10. 1-b quantizer as part of the bandpass 1-b Σ/Δ modulator in Fig. 7.

noise $n(k)$ is assumed to be random, zero-mean white, and orthogonal to the sinusoidal signal [19]–[22]. This assumption is further supported here by the presence of the random dithering sequence $d(k)$ which is, by construction, independent of any other sequence. The orthogonality between the quantization noise and the sinusoidal signal implies that all the signals in the loop are decomposed into a sinusoidal plus a noise [random wide sense stationary (WSS)] signal component.[1] This decomposition allows us to derive a *quasi-linear*[2] model of the modulator and capture its behavior more accurately than with the simple model of the linearized quantizer.

Based on the above, we assume that the quantizer's input $e(k)$ in Fig. 10 is written as $e(k) = e_c(k) + e_n(k)$, where $e_n(k)$ is zero-mean WSS Gaussian random noise with standard deviation σ_{e_n} [19], [22]. In addition, $e_c(k) = C\cos(k\Omega + \varphi)$ is a sinusoidal of fixed amplitude C and random phase φ, which is uniformly distributed in $[0, 2\pi]$. As $e_c(k)$ is a function of the random variable φ, it is a random variable as well. It can be verified that the range of $e_c(k)$ is $[-C, C]$ with probability density function $f_{e_c}(v) = 1/\left(\pi\sqrt{C^2 - v^2}\right)$. Finally, our orthogonality assumptions imply

$$\mathop{E}_{e_n(k), e_c(k)}\left\{e_n(k)e_c(k)\right\} = 0. \tag{4}$$

The *quasi-linearization* of the quantizer requires that we also express the output $x(k) = \operatorname{sgn}\big(e(k)\big)$ as a sum of the input components $e_c(k)$ and $e_n(k)$ weighted by some gain factors K and L, respectively, plus an additional quantization noise (error) $n(k)$, that is

$$x(k) = Ke_c(k) + Le_n(k) + n(k). \tag{5}$$

Equivalently we can define the quantization noise using $n(k) \triangleq \operatorname{sgn}\big(e(k)\big) - [Ke_c(k) + Le_n(k)]$. The above are illustrated graphically in Fig. 11, where the quantizer is modeled by two separate paths, one for the noise and the other for the sinusoidal signal, implying that $x_n(k) = Le_n(k) + n(k)$ and $x_c(k) = Ke_c(k)$. Block "S" for *splitter* is used only for pictorial representation of the signals' separation.

Gain factors K and L are selected to minimize the mean-square of the quantization noise $n(k)$ with respect to both random variables $e_n(k) \sim N(0, \sigma_{e_n}^2)$ and $e_c(k) \sim f_{e_c}$, i.e., they solve the minimization problem $\min\limits_{L,K} \mathop{E}\limits_{e_n(k), e_c(k)} \left\{n(k)^2\right\}$ [19], [22]. From the Appendix, we get

$$K = \sqrt{\frac{2}{\pi\sigma_{e_n}^2}} \cdot M\left(\frac{1}{2}, 2, -\rho^2\right) \tag{6}$$

[1] The accuracy of this decomposition depends on the loop parameters and the amplitude of the input sinusoidal as well as on the dither's power.

[2] For the definition of *quasilinearization*, the procedure of *statistical linearization* and the use of random-input describing functions (RIDFs) the reader is referred to [19].

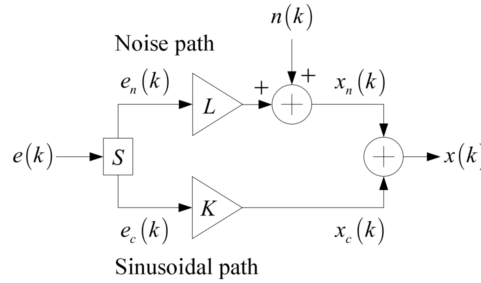

Fig. 11. Quasi-linear model of the quantizer in Fig. 10.

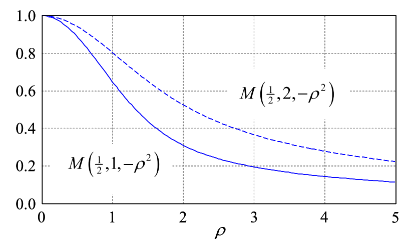

Fig. 12. Kummer functions $M\left(\frac{1}{2}, 1, -\rho^2\right)$ and $M\left(\frac{1}{2}, 2, -\rho^2\right)$.

and

$$L = \sqrt{\frac{2}{\pi\sigma_{e_n}^2}} \cdot M\left(\frac{1}{2}, 1, -\rho^2\right) \tag{7}$$

where ρ is the square root of the *signal* $e_c(k)$ *power*, $C^2/2$ divided by the *noise* $e_n(k)$ *power*, $\sigma_{e_n}^2$, i.e., the SNR at the input of the quantizer

$$\rho = \frac{C}{\sqrt{2}\sigma_{e_n}} \tag{8}$$

$M(a, b, z)$ is Kummer's (confluent hypergeometric) function [23] which can be expressed as

$$M(a, b, z) = \sum_{n=0}^{\infty} \frac{a(a+1)\ldots(a+n-1)}{b(b+1)\ldots(b+n-1)} \cdot \frac{z^n}{n!}. \tag{9}$$

Henceforth, we assume that K and L always have the values given by (6) and (7), respectively. Note, however, that parameters ρ and σ_{e_n} are still undetermined; their values are derived in the following section by solving the complete set of algebraic equations describing the loop. Also note that functions $M(\frac{1}{2}, 1, -\rho^2)$ and $M(\frac{1}{2}, 2, -\rho^2)$ *decrease* with the SNR ρ, as shown in Fig. 12. The same is true for K and L as functions of ρ, assuming σ_{e_n} is fixed.

The difference between the quasi-linear approach to the simple linearization of the quantizer is that here, we assume different gain factors K and L for the sinusoidal and the noise component, respectively, which also depend on the power of the two components.

B. Quasi-Linear Model of the Modulator

By replacing the quasi-linear model of the quantizer into the modulator we get the quasi-linear model of the latter shown

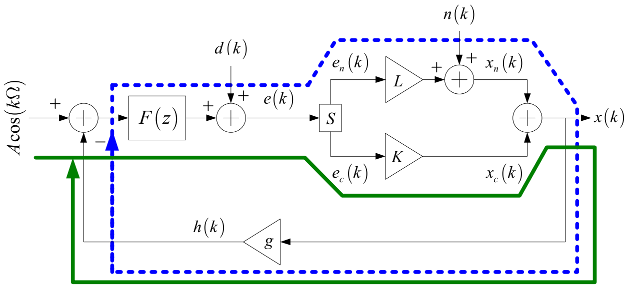

Fig. 13. Quasi-linear model of the modulator with the flow of the sinusoidal (thick solid line) and the noise (thick dashed line) signals.

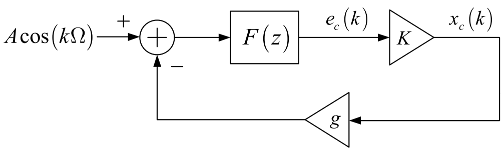

Fig. 14. Sinusoidal signal loop of Fig. 13.

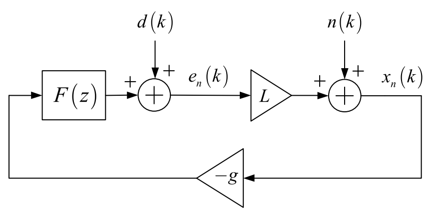

Fig. 15. Noise signal loop of Fig. 13.

in Fig. 13. Here, the sinusoidal and the noise signals flow in parallel inside the loop and they interact only via the nonlinear algebraic equations (6)–(8).

The sinusoidal and noise signal loops are shown separately in Figs. 14 and 15 and are analyzed parametrically with respect to K and L. The two-loop decomposition is similar to that in [22], however, here we have the additional random dither source $d(k)$ making the analysis more involved.

Setting $u(k) = A\cos(k\Omega)$ for the input of the sinusoidal signal loop, we get $X_c(z)/U(z) = KF(z)/\bigl(1 + gKF(z)\bigr)$ where $U(z)$ is the Z-transform of $u(k)$. A simplifying assumption, which is valid in most Σ/Δ modulators, is that the loop filter $F(e^{j\omega})$ has very high or infinite gain at the frequency of interest $\pm\Omega$, i.e., $\lim_{\omega\to\pm\Omega}|F(e^{j\omega})| = \infty$. The implication of this is

$$x_c(k) = \frac{A}{g}\cos(k\Omega). \tag{10}$$

From Fig. 14, we have $x_c(k) = Ke_c(k)$, which along with our assumption $e_c(k) = C\cos(k\Omega + \varphi)$ and (10) give $C = A/(gK)$ and $\varphi = 0$. Hence, it is

$$K = A/(gC). \tag{11}$$

Combining (6) with (11) and using the definition of SNR metric ρ in (8), we get

$$\frac{\pi A^2}{4g^2} = \rho^2 M\left(\frac{1}{2}, 2, -\rho^2\right)^2. \tag{12}$$

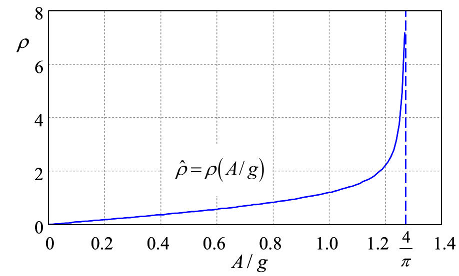

Fig. 16. Solution $\rho = \hat{\rho}(A/g)$ of (12).

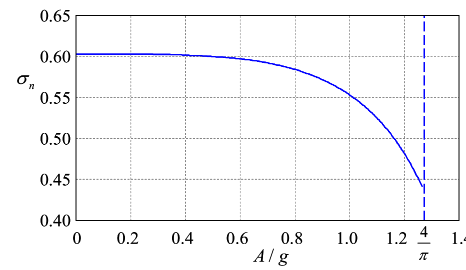

Fig. 17. Standard deviation σ_n as a function of A/g.

Equation (12) involves modulator's gain g and input's amplitude A parameters as well as unknown ρ for which it can be solved. Function $\rho^2 M(1/2, 2, -\rho^2)^2$ is strictly increasing for $\rho \geq 0$ and such that $\lim_{\rho\to\infty}\rho^2 M(1/2, 2, -\rho^2)^2 = 4/\pi$. Therefore, (12) has a real (nonnegative) solution if and only if $A/g < 4/\pi$ and the solution is unique. The solution, call it $\hat{\rho}(A/g)$, as a function of A/g is shown in the graph of Fig. 16. Throughout the rest of this paper it is assumed that $A/g < 4/\pi$ and $\rho = \hat{\rho}(A/g)$.

Next, we derive the power of the quantization noise $\sigma_n^2 \triangleq E\{n(k)^2\}$ following [22]. To this end we use (5), the definition $x(k) = \operatorname{sgn}\bigl(e(k)\bigr)$, the fact that $n(k)$ is orthogonal to $e_c(k)$ and $e_n(k)$ as shown in (24) and the implied orthogonality between $e_c(k)$ and $e_n(k)$ in (4) according to our assumptions, to get

$$1 = E\left\{x(k)^2\right\} = K^2 E\left\{e_c(k)^2\right\} + L^2 E\left\{e_n(k)^2\right\} + \sigma_n^2.$$

Replacing $E\{e_c(k)^2\} = C^2/2$, $E\{e_n(k)^2\} = \sigma_{e_n}^2$ as well as K and L from (6) and (7), and using (8) and (12) we conclude that

$$\sigma_n^2 = 1 - \frac{A^2}{2g^2} - \frac{2}{\pi}M\left(\frac{1}{2}, 1, -\rho^2\right)^2. \tag{13}$$

Solving (12) for ρ as a function of A/g, and replacing it in (13) we derive the standard deviation σ_n as a function of A/g. The graph is shown in Fig. 17.

Based on our assumptions, signals $e_n(k)$, $d(k)$, and $n(k)$ are WSS and so we can use the standard definition of the PSD. For example, the PSD of the noise signal $e_n(k)$ is $S_{e_n}(\omega) = \sum_{k=-\infty}^{\infty} R_{e_n}(k)e^{-k\omega j}$ where $R_{e_n}(k)$ is the autocorrelation function, i.e., $R_{e_n}(k) = E\bigl\{e_n(m+k)e_n(m)\bigr\}$. For the inverse we have $2\pi R_{e_n}(k) = \int_{-\pi}^{\pi} S_{e_n}(\omega)e^{k\omega j}d\omega$ and in particular, the variation of $e_n(k)$ can be expressed as

$$\sigma_{e_n}^2 = R_{e_n}(0) = \frac{1}{2\pi}\int_{-\pi}^{\pi} S_{e_n}(\omega)d\omega. \tag{14}$$

Taking the Z-transform of the signals in Fig. 15 we get

$$E_n(z) = \frac{1}{1+gLF(z)}D(z) - \frac{gF(z)}{1+gLF(z)}N(z). \tag{15}$$

Equation (15) and the stochastic independence between dithering $d(k)$ and noise $n(k)$ imply that [24]

$$S_{e_n}(\omega) = \left|\frac{1}{1+gLF(e^{j\omega})}\right|^2 S_d(\omega) + \left|\frac{gF(e^{j\omega})}{1+gLF(e^{j\omega})}\right|^2 S_n(\omega). \tag{16}$$

As mentioned in Section III-A, we adopt the typical assumption that $n(k)$ is zero-mean white [19]–[22]. This is approximately true under certain conditions [25]–[28] and the presence of white Gaussian dither $d(k)$ here supports it further by randomizing the quantization error. Therefore, the PSD of $n(k)$ is $S_n(\omega) = \sigma_n^2$ where σ_n is derived from (13). Also, the PSD of $d(k)$ is by construction $S_d(\omega) = \sigma_d^2$.

Noise $x_n(k)$ passes through the linear filter $F(z)$ and assuming the latter introduces sufficient mixing, the output of the filter is approximately Gaussian. Moreover $d(k)$ is Gaussian by construction and so $e_n(k)$ is also approximately Gaussian. Equations (14) and (16) lead to

$$\begin{aligned}\sigma_{e_n}^2 = \frac{\sigma_d^2}{2\pi}&\int_{-\pi}^{\pi}\left|\frac{1}{1+gLF(e^{j\omega})}\right|^2 d\omega \\ &+\frac{\sigma_n^2}{2\pi}\int_{-\pi}^{\pi}\left|\frac{gF(e^{j\omega})}{1+gLF(e^{j\omega})}\right|^2 d\omega\end{aligned} \tag{17}$$

which has two unknowns, σ_{e_n} and L, since σ_d is a design parameter and σ_n has been derived from (13). Solving (7) for the standard deviation σ_{e_n} of the noise e_n we have

$$\sigma_{e_n} = \sqrt{\frac{2}{\pi}}\cdot\frac{M\left(\frac{1}{2},1,-\rho^2\right)}{L}. \tag{18}$$

Replacing it in (17) gives

$$\begin{aligned}\frac{4}{L^2}\cdot M\left(\frac{1}{2},1,-\rho^2\right)^2 = \sigma_d^2&\int_{-\pi}^{\pi}\left|\frac{1}{1+gLF(e^{j\omega})}\right|^2 d\omega \\ &+\sigma_n^2\int_{-\pi}^{\pi}\left|\frac{gF(e^{j\omega})}{1+gLF(e^{j\omega})}\right|^2 d\omega.\end{aligned} \tag{19}$$

The only unknown in (19) is L. Note, however, that the dependence of the right-hand side of (19) on L is quite involved and only numerical solutions are possible for most transfer functions $F(z)$. Deriving ρ from (12), σ_n from (13) and L from (19) we can find σ_{e_n} via (18).

Now we have all the algebraic equations needed to derive the parameter values of the two loops of the modulator's quasi-linear model. The procedure is summarized in Table II.

The resulting values of K and L from solving the system equations in Table II depend on filter $F(z)$ and the design parameters A, g, and σ_d. Choosing the values of the latter we can adjust K and L, and shape the behavior of the modulator to a certain extent.

TABLE II

DERIVATION OF MODULATOR'S QUASI-LINEAR MODEL PARAMETERS

1) Eq. (12)	$\Rightarrow\ \rho$
2) Eq. (13)	$\Rightarrow\ \sigma_n$
3) Eq. (19)	$\Rightarrow\ L$
4) Eq. (18)	$\Rightarrow\ \sigma_{e_n}$
5) Eq. (6)	$\Rightarrow\ K$

C. Modulator's Signal, Dither, and Noise Transfer Functions

From Fig. 13, we have $X(z) = X_c(z) + X_n(z)$. In addition, from the sinusoidal and noise signal loops in Figs. 14 and 15, respectively, we get that

$$\begin{aligned}X_c(z) &= STF(z)U(z)\\ X_n(z) &= DTF(z)D(z) + NTF(z)N(z)\end{aligned} \tag{20}$$

where the *signal, dither,* and *noise transfer functions*, in the sense of the quasi-linear approximation, are

$$\begin{aligned}STF(z) &= \frac{KF(z)}{1+gKF(z)}\\ DTF(z) &= \frac{L}{1+gLF(z)}\end{aligned}$$

and

$$NTF(z) = \frac{1}{1+gLF(z)}$$

respectively.[3] Therefore, the output noise component of the modulator $X_n(z)$ has PSD given as

$$\begin{aligned}S_{X_n}(\omega) &= \left|DTF(e^{j\omega})\right|^2 S_d(\omega) + \left|NTF(e^{j\omega})\right|^2 S_n(\omega)\\ &= \left|DTF(e^{j\omega})\right|^2 \sigma_d^2 + \left|NTF(e^{j\omega})\right|^2 \sigma_n^2.\end{aligned} \tag{21}$$

Finally, adding (20) gives the total output of modulator's quasi-linear model, that is

$$X(z) = STF(z)U(z) + DTF(z)D(z) + NTF(z)N(z). \tag{22}$$

D. Stability of the Modulator's Quasi-Linear Model

For the quasi-linear model of the modulator to be meaningful, both noise and signal loops in Figs. 14 and 15 with transfer functions $NTF(z)$ and $STF(z)$, respectively, need to be stable.[4] Since $|F(z)|$ must take large values within the band of interest around Ω, to make $\left|DTF(z)\right|$, $|NTF(z)| \simeq 0$ and $|STF(z)| \simeq 1/g$, it is reasonable to select $F(z)$ with poles on the unit circle, on and near $e^{\pm j\Omega}$.

The stability of $NTF(z)$ and $STF(z)$ means that for the selected value of g and the resulting values of K and L, the poles of $NTF(z)$ and $STF(z)$, i.e., the roots of

$$1 + gLF(z) \quad \text{and} \quad 1 + gKF(z) \tag{23}$$

are inside the unit circle. Therefore, we have to derive first the range of gL and gK leading to stable transfer functions; then

[3]Note that $NTF(z)$ and $STF(z)$ here are different than those derived using the simple model of the modulator in (1)-(2).

[4]Note that the stability of $NTF(z)$ implies that of $DTF(z)$.

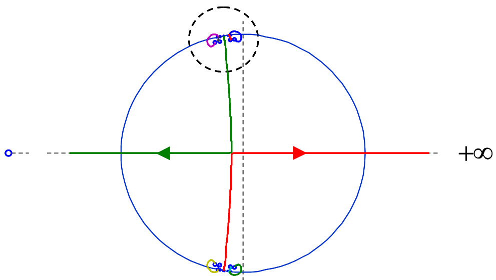

Fig. 18. Root locus of $1+rF(z)$ with respect to parameter r in the example of $F(z)$ in (3) and Table I.

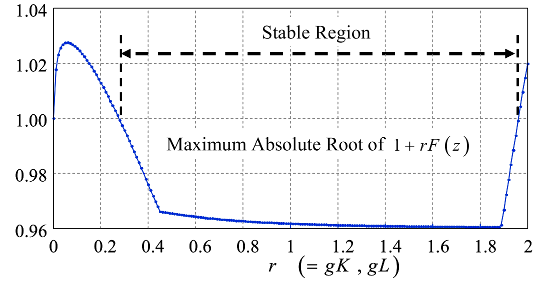

Fig. 20. Maximum absolute value of the roots of $1+rF(z)$.

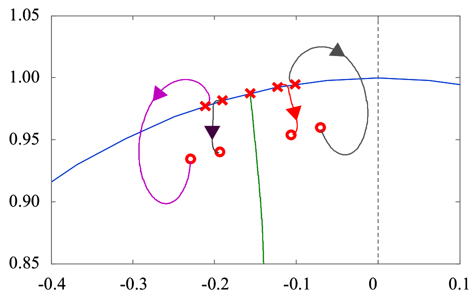

Fig. 19. Zoomed-in view of the root locus in Fig. 18.

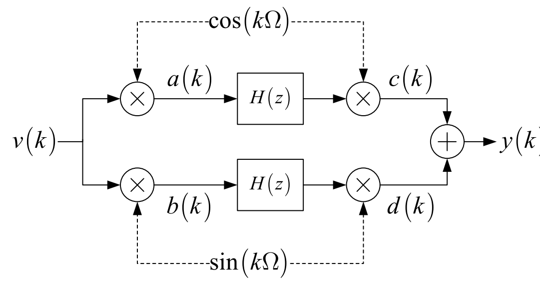

Fig. 21. Quadrature homodyne implementation of $F(z)$.

select g so that the equations in Table II have solution(s) for L and K resulting in gL and gK within the corresponding ranges of stability.

Let $F(z) = P(z)/Q(z)$ where $P(z)$ and $Q(z)$ are polynomials of orders m_n and m_d, respectively. Since $F(z)$ is located inside the loop in Fig. 7 it must be $m_n < m_d$ for the loop to be realizable [20].

Using r to denote both gL and gK, the root locus theory states that: 1) the root locus of $1+rF(z)$ begins from the poles of $F(z)$, for $r = 0^+$ and 2) m_n of the roots tend to the zeros of $F(z)$ and the remaining $m_d - m_n$ tend to infinity as $r \to \infty$. Given that $m_d - m_n > 0$, for large values of $r = gL, gK$ the polynomials in (23) have roots outside the unit circle. The root locus of the example of $F(z)$ in (3) and Table I is shown in Fig. 18. Note that one root approaches $+\infty$ and another one exits the unit circle to approach the zero at $-7.4398 + 0j$ as $r \to \infty$.

A zoomed-in view of the circled area in Fig. 18 is shown in Fig. 19 revealing that two of the poles depart from their initial position towards the outside of the unit circle. Hence, both the small and large values of r lead to instability. This case is rather typical and one has to resort to either direct calculation of the poles as a function of r or to use other tools like Jury's criterion [29].

Fig. 20 shows the maximum absolute value of the roots of $1 + rF(z)$, following the example of $F(z)$ in (3) and Table I, indicating the range of stability of r. For a more detailed treatment of the stability of Σ/Δ modulators based on quasi-linear modeling the reader is referred to [30]–[32].

IV. Quadrature Homodyne Filter

The loop transfer function $F(z)$ must result in $NTF(z)$ and $DTF(z)$ with band-stop behavior. To this end, $|F(z)|$ must attain large values in the band of interest around Ω as in Fig. 8(A). Typically, the bandpass filter $F(z)$ is derived from a low-pass one via transformations that result in twice the order. The choice of the filter's topology and numerical accuracy (number of bits) needed to represent the state variables and implement the summations and multiplications are important. Filters with high attenuation and high order require accurate placement of poles and zeros.

In many applications, the tunability of $F(z)$ is desirable in order to center the noise-suppressed band of $NTF(z)$ and $DTF(z)$ at the generated frequency Ω. Tunability in a direct implementation of $F(z)$ requires that the coefficients of the denominator and the numerator of $F(z)$ vary with Ω. Such variations heavily constrain the potential tradeoffs between the accuracy and computational cost reduction.

An alternative way is proposed here to realize the tunable bandpass transfer function $F(z)$, *always centered at the generated frequency* Ω, using two fixed identical low-pass filters $H(z)$ of half the order of $F(z)$. It offers the advantage of a fixed filter to trade accuracy for complexity reduction. The concept is illustrated in Fig. 21 where the $\cos(k\Omega)$ and $\sin(k\Omega)$ streams are generated by the LUT of the synthesizer simultaneously with the modulator's input.

As $v(k)$ is a sinusoidal or a modulated carrier centered at frequency Ω, the filter can be viewed as a quadrature homodyne down-conversion of $v(k)$ to baseband, low-pass filtering, and then up-conversion back to frequency Ω. Using basic properties of the Z-transform we get from Fig. 21

$$A\left(e^{j\omega}\right) = \frac{1}{2}\left[V\left(e^{j(\omega-\Omega)}\right) + V\left(e^{j(\omega+\Omega)}\right)\right]$$
$$B\left(e^{j\omega}\right) = \frac{1}{2i}\left[V\left(e^{j(\omega-\Omega)}\right) - V\left(e^{j(\omega+\Omega)}\right)\right]$$

TABLE III
POLES AND ZEROS OF EXAMPLE TRANSFER FUNCTION $H(z)$

POLES	ZEROS
1.0000	-
0.9985 ± 0.0553j	0.9589 ± 0.0452j
0.9994 ± 0.0346j	0.9565 ± 0.0813j

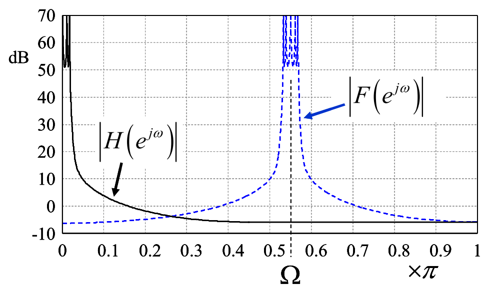

Fig. 22. Amplitude response of the low-pass $H(z)$ and that of the corresponding quadrature homodyne bandpass $F(z)$.

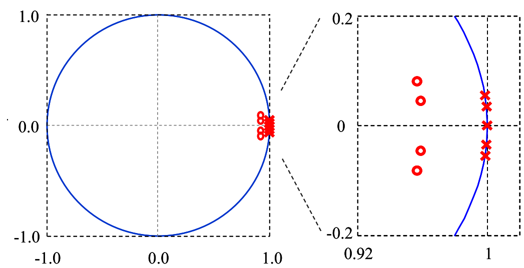

Fig. 23. Poles and zeros of the example low-pass function $H(z)$.

implying

$$C\left(e^{j\omega}\right) = \frac{1}{2}\Big[H\left(e^{j(\omega-\Omega)}\right)A\left(e^{j(\omega-\Omega)}\right) + H\left(e^{j(\omega+\Omega)}\right)A\left(e^{j(\omega+\Omega)}\right)\Big]$$

$$D\left(e^{j\omega}\right) = \frac{1}{2i}\Big[H\left(e^{j(\omega-\Omega)}\right)B\left(e^{j(\omega-\Omega)}\right) - H\left(e^{j(\omega+\Omega)}\right)B\left(e^{j(\omega+\Omega)}\right)\Big].$$

Adding them, $Y\left(e^{j\omega}\right) = \left[H\left(e^{j(\omega-\Omega)}\right) + H\left(e^{j(\omega+\Omega)}\right)\right] V\left(e^{j\omega}\right)/2$ which following the definition $F(z) \equiv Y(z)/V(z)$ gives:

$$F(z) = \frac{1}{2}\Big[H\left(ze^{-j\Omega}\right) + H\left(ze^{j\Omega}\right)\Big].$$

Therefore, $F(z)$ is the sum of two replicas of $H(z)$, frequency shifted by $\pm\Omega$, respectively.

The poles and zeros of $H(z)$ corresponding to $F(z)$ in (3) and Table I are given in Table III and the gain of $H(z)$ is one. Fig. 22 shows the Bode plot of the low-pass transfer function $H(z)$ and that of the bandpass one $F(z)$.

The five poles and four zeros of the low-pass $H(z)$ are at and around $1 + 0j$ as shown in Fig. 23. The poles and zeros of the bandpass $F(z)$ are shown in Fig. 9.

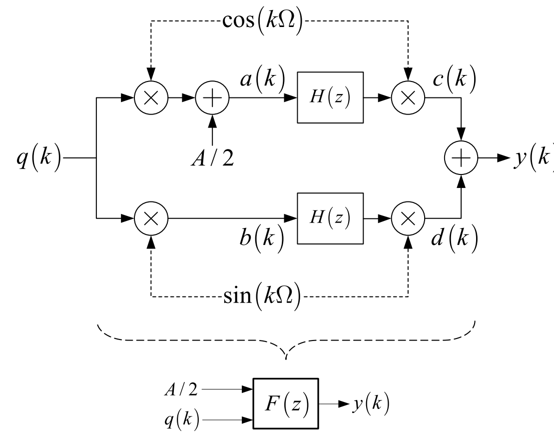

Fig. 24. IMQH filter $F(z)$ with input $q(k) = -gx(k)$ and parameter $A/2$ replacing the input component $A\cos(k\Omega)$ of the quadrature homodyne in Fig. 21.

A. Multiplier-Free Quadrature Homodyne Filter

Consider the quadrature homodyne filter in Fig. 21, which is a carrier-centered (Ω) realization of $F(z)$ in the modulator in Fig. 7. The quadrature homodyne filter appears to have four extra multipliers, raising the hardware complexity of the modulator. It is shown next that the two input multipliers can be eliminated directly and the two output ones can be replaced by operators of trivial hardware complexity with minimal or no cost on the output spectrum.

Observe from Fig. 7 that the input to $F(z)$ in Fig. 21 is the sum $v(k) = A\cos(k\Omega) - gx(k)$. Consider only the first component, i.e., let for the moment be $v(k) = A\cos(k\Omega)$, assuming $x \equiv 0$, and note that in this case in Fig. 21, it is $a(k) = A/2 + (A/2)\cos(2\Omega k)$ and $b(k) = (A/2)\sin(2\Omega k)$. Since $H(z)$ is lowpass it is reasonable to assume that both frequencies 2Ω and its alias $2\pi - 2\Omega$ are outside the bandwidth of $H(z)$. Therefore, the impact of $A\cos(k\Omega)$ on the filter's output $Y(z) = F(z)X(z)$ is essentially identical to adding $A/2$ after the input cosine multiplication. This is shown in Fig. 24 where the input here is $q(k) = -gx(k)$ and $A/2$ is considered as a parameter. We refer to the filter structure in Fig. 24 as the *input-modified quadrature homodyne* (IMQH) filter.

Replacing the IMQH filter of Fig. 24 in the Σ/Δ modulator of Fig. 7, we get the scheme in Fig. 25. Here, A is a static or slowly varying modulation and the main input to the filter is $q(k) = -gx(k)$, which takes only the two values $\pm g$.

Factor g was introduced to allow trimming the stability of the modulator and can be absorbed into $H(z)$ or it can be 2^m, for some integer m, which is implemented without computational cost. Therefore, the two input multiplications (down-conversion) in Fig. 24 are essentially multiplications by ± 1 and therefore of no cost.

Regarding the other two multipliers at the output (up-conversion) of the filter in Fig. 24, it has been observed empirically that the in-band spectrum of the modulator remains almost unchanged when $\cos(k\Omega)$ and $\sin(k\Omega)$ are quantized in three levels $0, \pm 1$ with threshold values of $\pm\eta$ (typically $\eta = 1/2$) as captured by the quantizing function Q_3 in Fig. 26.

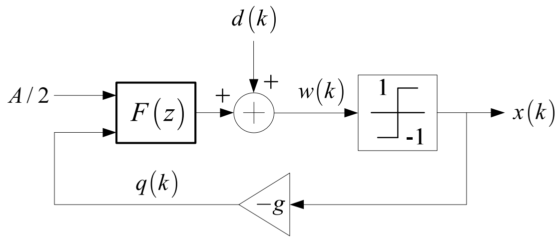

Fig. 25. Bandpass 1-b Σ/Δ modulator with the IMQH filter implementation of $F(z)$ in Fig. 24.

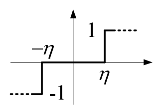

Fig. 26. Three-level quantizing function Q_3.

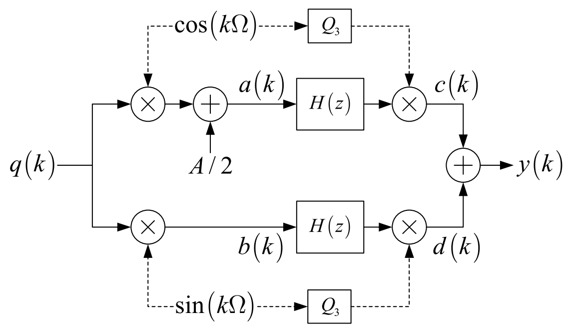

Fig. 27. MF-IMQH filter with input $q(k) = -gx(k)$, $g = 2^m$, and $A/2$.

The IMQH filter in Fig. 24 is replaced by that in Fig. 27, which is essentially *multiplier-free* (MF) as all the four multiplications are by 0, ±1 only.

The architecture of the bandpass 1-b Σ/Δ modulator using the MF-IMQH filter is identical to that in Fig. 25 but with filter $F(z)$ implemented as in Fig. 27. Output spectra comparison of the modulator using the regular (IMQH) and the MF-IMQH filters in Figs. 24 and 27, respectively, are presented in Section V.

V. Simulation Results and Final Remarks

The developed theory provides the tools to design the modulator for single-bit all-digital frequency synthesis with stable operation and to predict the sinusoidal amplitude and the PSD of the noise at the output. The following examples compare the theoretical estimates with the simulation results derived using MATLAB/SIMULINK.

Example 1: The proposed single-bit all-digital frequency synthesizer based on the Σ/Δ modulator in Fig. 25 is implemented using the IMQH architecture in Fig. 24. The poles and zeros of the low-pass transfer function $H(z)$ are shown in Table III and its gain is one. The remaining loop and simulation parameters are shown in Table IV.

The simulated output spectrum is the dark (noisy blue) line in Fig. 28. The smooth gray line is the derived noise spectrum based on the developed theory. The x-axis can be read as $\times\pi$

TABLE IV

System and Simulation Parameters of Example 1

PARAMETER	VALUE
Frequency, Ω	$2\pi(2253/8192)$
Input Amplitude, A	0.5
Loop Auxiliary Gain, g	1
Dither's standard deviation, σ_d	0.3
Simulated steps in SIMULINK	1.5×10^6
Output PSD vector length	327680
Equivalent Clock Frequency/Resolution BW	1 GHz / 3052 Hz

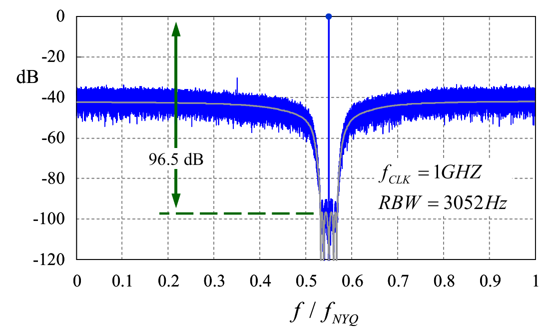

Fig. 28. Output spectrum of the all-digital frequency synthesizer using the 1-b Σ/Δ modulator in Fig. 25 with the IMQH filter in Fig. 24. The poles and zeros of $H(z)$ are given in Table III and the loop parameters are given in Table IV.

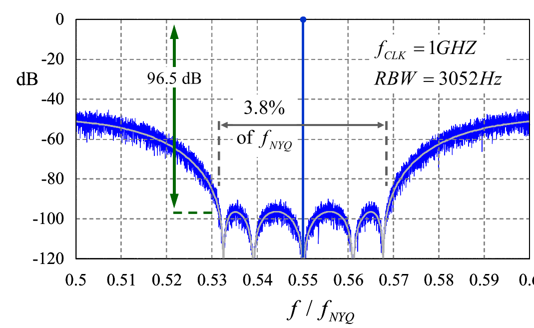

Fig. 29. Zoomed-in view of the output spectrum in Fig. 28.

or as $\times f_{\text{NYQ}}$ if we consider the output in the continuous time domain where $f_{\text{NYQ}} = f_{\text{CLK}}/2$.

Similarly, the number of 327 680 sequential output samples of $x(k)$ used to derive the spectrum can be viewed as having clock frequency $f_{\text{CLK}} = 1$ GHz and resolution bandwidth (RBW) equal to $f_{\text{CLK}}/327680 \cong 3052$Hz. In this RBW, the in-band noise is at about −96 dBc and no spurs appear in-band. Extrapolating, we can estimate an in-band DR of $96 + 10\log_{10}(\text{RBW}) \cong 131$ dBc/Hz. Note that the achieved in-band DR in dBc/Hz is a function of f_{CLK}, i.e., of the processing gain $10\log_{10}(f_{\text{CLK}})$.

An in-band zoomed-in view shown in Fig. 29 indicates the width of the usable range to be about 3.8% of $f_{\text{NYQ}} = f_{\text{CLK}}/2$.

Since the bandpass Σ/Δ modulator can suppress spurs and noise only within the bandwidth of its loop filter $F(z)$, if

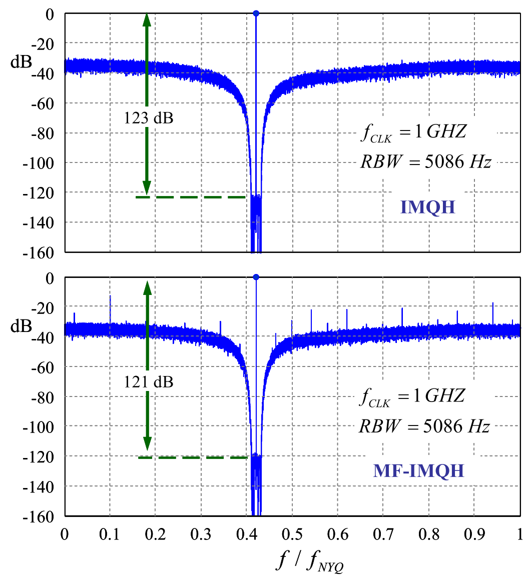

Fig. 30. Output spectrum. Top: using the IMQH filter in Fig. 24. Bottom: using the MF-IMQH filter in Fig. 27.

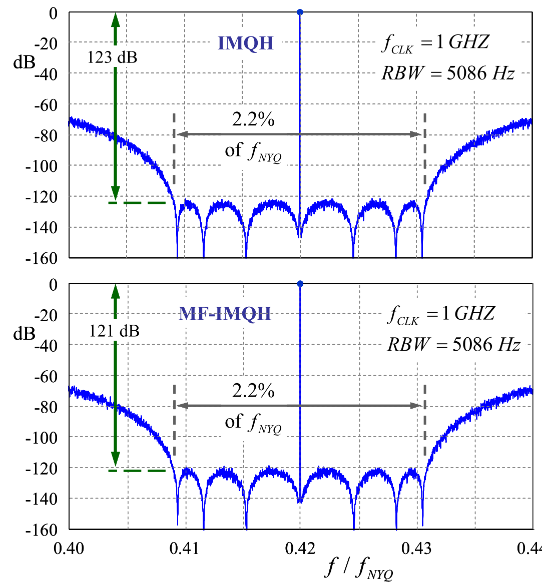

Fig. 31. Zoomed-in view of the output spectra in Fig. 30.

out-of-band spectral clarity is important one has to employ additional circuit techniques to suppress the noise and spurs as well. For example, the use of a surface acoustic wave filter following the modulator can be very effective. If the modulator is part of a chain, the inherent bandpass behavior of following blocks like tuned amplifiers or tuned mixers may be adequate. For instrumentation systems, a clean-up PLL [33]–[35] may be a more appropriate choice.

Example 2: Here we compare the output spectrum of the two cases using the IMQH filter in Fig. 24 and using its MF-IMQH variation in Fig. 27. In the second case, extra attention in the stability is required as the MF variation introduces additional nonlinearities that alter slightly the effective filter gain and therefore the gain of the loop.

A narrower low-pass filter $H(z)$ of seventh order is used and the length of the output vector used corresponds to resolution bandwidth RBW $=$ 5.086 kHz if a clock frequency of $f_{\text{clk}} = 1$ GHz is assumed. Fig. 30 presents the two spectra, where both have in-band noise level below -121 dBc and no spurs appear in-band. Extrapolating again, we can estimate a DR in-band of about $121 + 10\log_{10}(5086) \cong 158$ dBc/Hz. In the case of the MF-IMQH filter, there are a number of spurs outside the band. Finally, in-band zoomed-in views of the spectra are shown in Fig. 31, indicating about 2.2% of f_{NYQ} of usable range and spurs-free operation in both the cases.

Minimal power consumption and maximum synthesizable frequency are most important. Multipliers are typically the most power and time-consuming blocks restricting performance. Comparison of the spectra in Figs. 30 and 31 indicates that replacing the IMQH filter with the multiplierless MF-IMQH one maintains the same in-band spectral quality.

Example 3: The Σ/Δ modulator in Fig. 25, with either the IMQH architecture in Fig. 24 or the MF-IMQH one in Fig. 27, typically produces a spurs-free in-band output without the need for dithering ($\sigma_d = 0$). There are

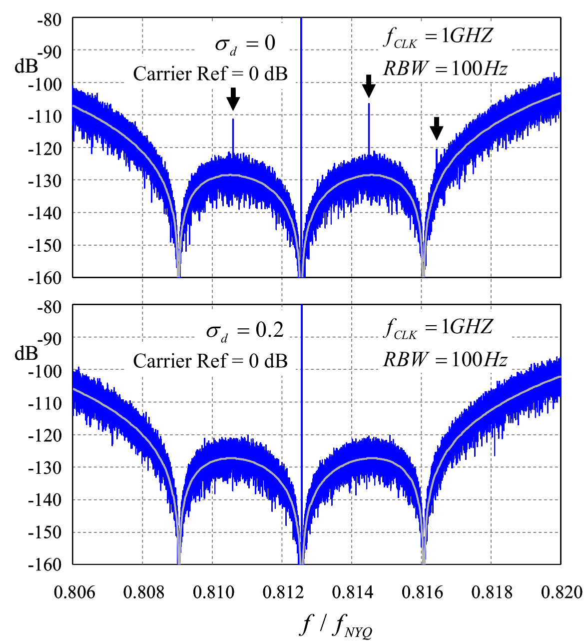

Fig. 32. Output spectrum. Top: without dithering ($\sigma_d = 0$). Bottom: with dithering $\sigma_d = 0.2$.

some rare cases, however, where small spurs may appear in-band and dithering can be used to suppress them and increase the SFDR. Consider the Σ/Δ modulator in Fig. 25 with the IMQH in Fig. 24 and the low-pass transfer function $H(z)$ of third order with unity gain, poles $0.999939 \pm 0.011048j$ and 1, and zeros $0.967773 \pm 0.030242j$. The remaining loop and simulation parameters are shown in Table V.

The spectra without dithering (top) and with dithering $\sigma_d = 0.2$ (bottom) are shown with a dark (noisy blue) line in Fig. 32. The smooth gray line is the estimated noise PSD based on the developed theory. Equivalent clock frequency and RBW are $f_{\text{CLK}} = 1$ GHz and RBW $\cong$ 100 Hz, respectively.

TABLE V
SYSTEM AND SIMULATION PARAMETERS OF EXAMPLE 3

PARAMETER	VALUE
Frequency, Ω	$2\pi(13313/32768)$
Input Amplitude, A	0.5
Loop Auxiliary Gain, g	1
Dither's standard deviation, σ_d	0 and 0.2
Simulated steps in SIMULINK	44990464
Output PSD vector length	9994240
Equivalent Clock Frequency/Resolution BW	1 GHz / 100 Hz

The three spurs on the top graph disappear when dithering is used (bottom). The cost of dithering is an increase in the noise level in simulation of about 1.4 dB at the peak of the two lobes. The corresponding theoretical estimate (smooth gray line) indicates an increase of about 1.2 dB.

VI. CONCLUSION

All-digital frequency synthesis with single-bit bandpass Σ/Δ modulation was presented as a mean of achieving spectrally clean sinusoidal-like single-bit output. A mathematical framework for predicting the modulator's stability and output spectrum was introduced. To alleviate the inherent tradeoff between tunability and complexity in the bandpass filter of the modulator, the quadrature homodyne filter architecture and its multiplier-free variation were introduced, both offering tunable bandpass response while using fixed low-pass filters. MATLAB–SIMULINK simulation results validate the theoretical analysis and illustrate the capability of this class of synthesizers to achieve very high dynamic range near-in.

APPENDIX

As $\underset{e_n(k),e_c(k)}{E}\{n(k)^2\}$ is independent of the time index k, we drop k for notational convenience and we consider all the expectations with respect to both e_n and e_c.

We observe that $E\{\text{sgn}(e_c+e_n)^2\} = 1$, $E\{e_c^2\} = C^2/2$ and we also have $E\{e_n^2\} = \sigma_{e_n}^2$ and $E\{e_n e_c\} = 0$ due to our assumptions and definitions in Section III-A. Using the above, we derive

$$\begin{aligned} E\left\{n^2\right\} &= E\left\{\left(\text{sgn}(e_c+e_n) - [Le_n + Ke_c]\right)^2\right\} \\ &= 1 + L^2\sigma_{e_n}^2 + K^2C^2/2 - 2LE\{\text{sgn}(e_c+e_n)e_n\} \\ &\quad - 2KE\{\text{sgn}(e_c+e_n)e_c\}. \end{aligned}$$

Setting the partial derivatives of $E\{n^2\}$ with respect to K, L

$$\begin{aligned} \frac{\partial E\left\{n^2\right\}}{\partial K} &= KC^2 - 2E\{\text{sgn}(e_c+e_n)e_c\} \\ \frac{\partial E\left\{n^2\right\}}{\partial L} &= 2L\sigma_{e_n}^2 - 2E\{\text{sgn}(e_c+e_n)e_n\} \end{aligned}$$

equal to zero results in the pair of $K = 2E\{\text{sgn}(e_c+e_n)e_c\}/C^2$ and $L = E\{\text{sgn}(e_c+e_n)e_n\}/\sigma_{e_n}^2$ which is the point of global minimum of $E\{n^2\}$, i.e., $\min_{L,K} \underset{e_n(k),e_c(k)}{E}\{n(k)^2\}$. Moreover, we note that (for this pair of K and L) it is

$$E\{n(k)e_c(k)\} = E\{n(k)e_n(k)\} = 0. \tag{24}$$

Writing explicitly the expressions for K and L we get

$$\begin{aligned} K = \frac{2}{C^2}\int_{-\infty}^{\infty}\int_{-C}^{C} p\,\text{sgn}(p+r)\frac{1}{\sqrt{2\pi\sigma_{e_n}^2}} \\ \times e^{-\frac{r^2}{2\sigma_{e_n}^2}}\frac{1}{\pi\sqrt{C^2-p^2}}dpdr \end{aligned}$$

and

$$\begin{aligned} L = \frac{1}{\sigma_{e_n}^2}\int_{-\infty}^{\infty}\int_{-C}^{C} r\,\text{sgn}(p+r)\frac{1}{\sqrt{2\pi\sigma_{e_n}^2}} \\ \times e^{-\frac{r^2}{2\sigma_{e_n}^2}}\frac{1}{\pi\sqrt{C^2-p^2}}dpdr \end{aligned}$$

which after some algebraic manipulation result in the compact expressions in (6) and (7) [22]. $M(a,b,z)$ is Kummer's (confluent hypergeometric) function [23], which can be expressed as in (9), which is convenient for numerical evaluation, or as

$$M(a,b,z) = \frac{\Gamma(b)}{\Gamma(a)\Gamma(b-a)}\int_0^1 e^{zu}u^{a-1}(1-u)^{b-a-1}du$$

valid for $\text{Re}(b) > \text{Re}(a) > 0$, which can be used to derive properties of related analytical expressions [23].

ACKNOWLEDGMENT

The author would like to thank the Associate Editor Dr. Aaron Partridge and the anonymous reviewers for their valuable comments, as well as, Mrs. Falia Mania for reviewing the manuscript.

REFERENCES

[1] V. S. Reinhardt, "Direct digital synthesizers," Hughes Aircraft Co, Space and Communications Group, Los Angeles, CA, USA, Tech. Rep., Dec. 1985.
[2] C. E. Wheatley, "Digital frequency synthesizer with random jittering for reducing discrete spectral spurs," U.S. Patent 4410954, Oct. 18, 1983.
[3] V. N. Kochemasov and A. N. Fadeev, "Digital-computer synthesizers of two-level signals with phase-error compensation," *Telecommun. Radio Eng.*, vols. 36–37, pp. 55–59, Oct. 1982.
[4] K. Galanopoulos and P. P. Sotiriadis, "Optimal dithering sequences for spurs suppression in pulse direct digital synthesizers," in *Proc. IEEE Int. Freq. Control Symp.*, May 2012, pp. 1–4.
[5] P. P. Sotiriadis, "Spurs-free single-bit-output all-digital frequency synthesizers with forward and feedback spurs and noise cancellation," *IEEE Trans. Circuits Syst. I*, vol. 63, no. 5, pp. 567–576, May 2016.
[6] H. Mair and L. Xiu, "An architecture of high-performance frequency and phase synthesis," *IEEE J. Solid-State Circuits*, vol. 35, no. 6, pp. 835–846, Jun. 2000.
[7] H. Mair, L. Xiu, and S. A. Fahrenbruch, "Precision frequency and phase synthesis," U.S. Patent 6329850, Dec. 11, 2001.
[8] D. E. Calbaza and Y. Savaria, "A direct digital periodic synthesis circuit," *IEEE J. Solid-State Circuits*, vol. 37, no. 8, pp. 1039–1045, Aug. 2002.
[9] P. P. Sotiriadis, "Theory of flying-adder frequency synthesizers—Part I: Modeling, signals' periods and output average frequency," *IEEE Trans. Circuits Syst. I*, vol. 57, no. 8, pp. 1935–1948, Aug. 2010.
[10] P. P. Sotiriadis, "Theory of flying-adder frequency synthesizers—Part II: Time- and frequency-domain properties of the output signal," *IEEE Trans. Circuits Syst. I*, vol. 57, no. 8, pp. 1949–1963, Aug. 2010.

[11] P. Sotiriadis, "Exact spectrum and time-domain output of flying-adder frequency synthesizers," *IEEE Trans. Ultrason., Ferroelect., Freq. Control*, vol. 57, no. 9, pp. 1926–1935, Sep. 2010.

[12] R. Schreier and M. Snelgrove, "Bandpass sigma-delta modulation," *Electron. Lett.*, vol. 25, no. 23, pp. 1560–1561, 1989.

[13] R. Huang, N. Lotze, and Y. Manoli, "On design a high speed sigma delta DAC modulator for a digital communication transceiver on chip," in *Proc. 11th EUROMICRO Conf. IEEE Digit. Syst. Design Archit., Methods Tools*, Sep. 2008, pp. 53–60.

[14] J. Sommarek, J. Vankka, J. Ketola, J. Lindeberg, and K. Halonen, "A digital modulator with bandpass delta-sigma modulator," in *Proc. IEEE European Solid State Circuits Conf.*, Sep. 2004, pp. 159–162.

[15] S. Lusahas, R. Schreier, and H.-S. Lee, "A 924MHz Output, 17.5MHz Bandwidth -70bBc IMD3 $S\Sigma\Delta$ DAC," in *Proc. IEEE Custom Integr. Circuits Conf.*, 2003.

[16] J. Keyzer, J. Hinrichs, M. Metzger, I. Iwamoto, I. Galton, and P. Asbeck, "Digital generation of RF signal for wireless communication with bandpass delta sigma modulation," in *IEEE MTT-S Dig.*, 2001, pp. 2127–2130.

[17] R. Schreier, "Noise-shaped coding," Ph.D. dissertation, Dept. Elect. Eng., Univ. Toronto, ON, Canada, 1991.

[18] J. Vankka, *Digital Synthesizers and Transmitters for Software Radio*, The Netherlands: Springer, 2005.

[19] A. Gelb and W. E. V. Velde, *Multiple-Input Describing Functions and Nonlinear Systems Design*, New York, NY, USA: McGraw-Hill, 1968.

[20] R. Schreier and G. C. Temes, *Understanding Delta-Sigma Data Converters*, Hoboken, NJ, USA: Wiley, 2005.

[21] G. I. Bourdopoulos, A. Pnevmatikakis, V. Anastassopoulos, T. L. Deliyannis, and D. S. Modulators, *Modeling, Design and Applications*. London, U.K.: Imperial College Press, 2003.

[22] S. Ardalan and J. Paulos, "An analysis of nonlinear behavior in delta—Sigma modulators," *IEEE Trans. Circuits Syst.*, vol. 34, no. 6, pp. 593–603, Jun. 1987.

[23] M. Abramowitz and I. A. Stegun, *Handbook of Mathematical Functions: With Formulas, Graphs, and Mathematical Tables*. New York, NY, USA: Dover, 1965.

[24] A. Papoulis and S. U. Pillai, *Probability, Random Variables and Stochastic Processes*, 4th ed. New York, NY, USA: McGraw-Hill, 2002.

[25] H. Smith, *Approximate Analysis of Randomly Excited Nonlinear Controls*. Cambridge MA, USA: MIT Press, 1966.

[26] A. Sripad and L. Snyder, "A necessary and sufficient condition for quantization errors to be uniform and white," *IEEE Trans. Acoust., Speech Signal Process.*, vol. 25, no. 5, pp. 442–448, Oct. 1977.

[27] B. Widrow, "Statistical analysis of amplitude-quantized sampled-data systems," *Trans. Amer. Inst. Electr. Engineers, Part II, Appl. Ind.*, vol. 79, no. 6, pp. 555–568, Jan. 1961.

[28] B. Widrow, I. Kollar, and M.-C. Liu, "Statistical theory of quantization," *IEEE Trans. Instrum. Meas.*, vol. 45, no. 2, pp. 353–361, Apr. 1996.

[29] E. I. Jury, *Theory and Application of the Z-Transform Method*. Hoboken, NJ, USA: Wiley, 1964.

[30] L. Risbo, "Stability predictions for higher-order Band-Pass $\Sigma\Delta$ modulators for dual sinusoidal inputs," in *Proc. IEEE Int. Symp. Circuits Syst.*, May 2010, pp. 541–545.

[31] J. A. E. P. van Engelen, "Stability analysis and design of bandpass sigma delta modulators," *Tijdschrift-Nederlands Elektronica Radiogenootschap*, vol. 64, no. 5, p. 240, 1999.

[32] M. H. H. Hafelt, "On the stability of a l-bit-quantized feedback system," in *Proc. ICASSP*, Washington, DC, USA, 1979, pp. 844–848.

[33] W. F. Egan, *Frequency Synthesis by Phase Lock*, 2nd ed. New York, NY, USA: Wiley, 1999.

[34] U. L. Rohde, *Microwave and Wireless Synthesizers: Theory and Design*, 1st ed. Singapore: Wiley, 1997.

[35] V. Manassewitsch, *Frequency Synthesizers*, 3rd ed. New York, NY, USA: Wiley, 1987.

Paul P. Sotiriadis (SM'09) received the Diploma degree in electrical and computer engineering from the National Technical University of Athens, Athens, Greece, in 1994, the M.S. degree in electrical engineering from Stanford University, Stanford, CA, USA, in 1996, and the Ph.D. degree in electrical engineering and computer science from the Massachusetts Institute of Technology, Cambridge, MA, USA, in 2002.

In 2002, he joined Johns Hopkins University, Baltimore, MD, USA, as an Assistant Professor of Electrical and Computer Engineering. In 2012, he joined the faculty of the Electrical and Computer Engineering Department, National Technical University of Athens. He has authored or coauthored more than 95 technical papers in IEEE journals and conferences, holds one patent, has several patents pending, and has contributed chapters to technical books. He has led several projects funded by U.S. organizations and has collaborations with industry and national labs. His current research interests include design, optimization, and mathematical modeling of analog and mixed-signal circuits, RF and microwave circuits, advanced frequency synthesis, biomedical instrumentation, and interconnect networks in deep-submicrometer technologies.

Dr. Sotiriadis has received several awards, including the Best Paper Award in the IEEE International Symposium on Circuits and Systems in 2007, the Best Paper Award in the IEEE International Frequency Control Symposium in 2012, and the Guillemin-Cauer Award from the IEEE Circuits and Systems Society in 2012. He is an Associate Editor of the IEEE TRANSACTIONS ON CIRCUITS AND SYSTEMS - I and the *IEEE Sensors Journal*, and has served as an Associate Editor of the IEEE TRANSACTIONS ON CIRCUITS AND SYSTEMS - II from 2005 to 2010, and has been a member of technical committees of many conferences. He is a Reviewer for many IEEE TRANSACTIONS and conferences and serves on proposal review panels.